Self-Assembly of Heptameric Nanoparticles Derived from Tag-Functionalized Phi29 Connectors

Dominik J. Green,[†,‡] Joseph C. Wang,[†] Feng Xiao,[§] Ying Cai,[§] Rod Balhorn,[‡] Peixuan Guo,[§] and R. Holland Cheng[†,*]

[†]Department of Molecular & Cellular Biology, University of California, Davis, California 95616, United States, [‡]Lawrence Livermore National Laboratory, Physical & Life Sciences Directorate, Livermore, California 94550, United States, and [§]Department of Biomedical Engineering, University of Cincinnati, Cincinnati, Ohio 45221, United States

ARTICLE

ABSTRACT The structure of an induced macromolecular assembly was characterized and found to consist of an ordered heptameric arrangement of recombinant phi29 gp10 connector molecules. Insertion of an N-terminal Strep-II/His_6 tag to the connectors led to the spontaneous formation of large nanoparticles that were distinct from free, wild-type phi29 connectors in both size and symmetry elements. The determination of single-molecule tomograms and image-averaged reconstructions allowed for the stoichiometric and topological characterization of the ordered assemblage, revealing that the nanoparticle is composed of five equatorial connectors arranged with pseudo-5-fold rotational symmetry, capped on its ends by two polar connectors. Additionally, all seven connectors are oriented with their narrower N-terminal necks into the nanoparticle core and wider C-terminal ends out toward the nanoparticle surface, a geometric arrangement accommodated by the shape complementarity of the conical connector profiles. A significant amount of conformational heterogeneity was detected, ranging from changes in overall nanoparticle diameter, to tilting of individual connectors, to variations in connector stoichiometry. Nevertheless, a stable, heptameric nanoparticle was resolved, revealing the significant potential of guided, peptide-mediated supramolecular self-assembly. With this construct, we anticipate the further design of variable N-terminal tags to allow for the generation of nanoparticles with tailored connector stoichiometry and topological arrangements. By modifying the surface-exposed C-terminal ends with application-appropriate moieties, the consistent structure and compact nature of these nanoparticles may prove beneficial in nanotechnological and nanomedical approaches.

KEYWORDS: self-assembly · peptide tag · phi29 · DNA motor · gp10 connector · conformational heterogeneity · MSA

The ability to predefine and directly specify biomolecular interactions is a significant goal sought within systems biology and in the development of functionalized nanodevices.[1−7] By having the ability to bring desired components together in a predictable and orientation-dependent manner, the generation of tailored macromolecular complexes will be an indispensable tool for nanomachine construction and their resulting applications. In order to achieve this goal, however, better understanding of the components involved in the formation, stabilization, and controlled breakdown of self-assembled complexes must be attained. A stable and well-defined system for studying self-assembly has been found in bacteriophage phi29, composed of an energy-driven motor-based DNA packaging system.[8] In this study, we utilize a component of the phi29 packaging system to analyze a self-assembling supramolecular complex whose formation is mediated by peptide extensions.[9−11]

Phi29 is known to infect the soil bacterium *Bacillus subtilis*.[12] One of its gene products, gp10, spontaneously oligomerizes into a rotationally symmetric dodecamer known as the connector or portal protein.[13,14] The connector has a tapered, conical shape, with a narrow N-terminus, a wide C-terminus, and a hollow internal core large enough to accommodate a molecule of double-stranded DNA.[15,16] The wide C-terminus of the connector inserts into the procapsid of phi29, while the N-terminus associates with a packaging RNA molecule (pRNA) and the GTPase gp16.[17] Together, this complex functions as a high-powered motor responsible for packaging of the phi29 prohead with its genomic DNA.[18] Approaches to using this motor system as a vehicle for therapeutic DNA delivery into cells has been undertaken, with initial steps geared toward directional insertion of the gp10 connector into the cell plasma membrane.[19,20] In previous studies, we constructed tag-functionalized[21] molecules of gp10 connectors by introducing N- and C-terminal Strep-II or His_6 peptide extensions.[22,23] Interestingly, the recombinant connectors with N-terminal extensions, but not C-terminal, were able to self-assemble into well-ordered 24 nm × 29 nm nanoparticles. Visually, these complexes closely matched the appearance of those

*Address correspondence to rhch@ucdavis.edu.

Received for review September 21, 2010 and accepted November 04, 2010.

Published online November 16, 2010.
10.1021/nn1024829

© 2010 American Chemical Society

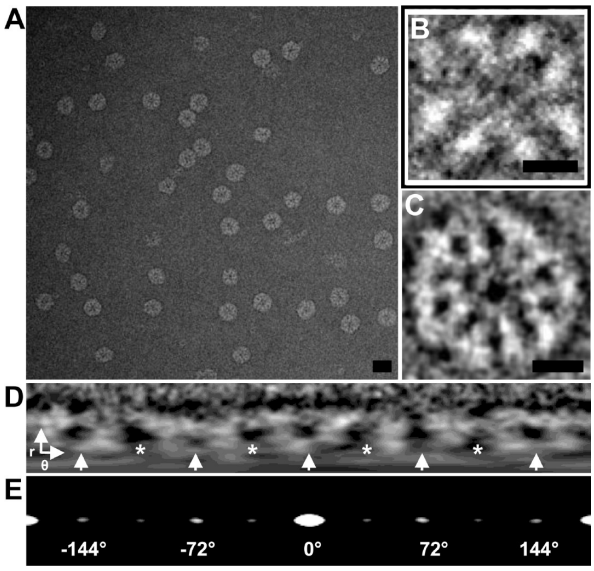

Figure 1. TEM image analysis of purified N-Strep/His nanoparticles. (A) Selected area from a micrograph of stain-embedded nanoparticles. Mostly intact nanoparticles can be seen; however, distorted nanoparticles and nanoparticle intermediates are also present. (B) Projection image of a nanoparticle in a side view orientation revealing horizontal (29 nm) and vertical (24 nm) near-mirror axes. (C) Projection image of a nanoparticle in a top view orientation revealing pseudo-five-fold rotational symmetry, with an overall diameter of 29 nm. (D) Polar transform of the top view projection in (C). Arrowheads indicate the location of EQC N-termini, while asterisks signify gaps between adjacent EQCs. A smear of density is present at low radii, indicating the presence of a POC. (E) Autocorrelation of the polar transform in (D). Peaks are found in 36° intervals, but brighter peaks are found every 72°. The brighter peaks correspond to alignment of the N-terminal neck regions (arrowheads) to one another (C_5-symmetric), whereas the fainter peaks suggest N-terminal neck alignment with the gaps (asterisks) between neighboring EQCs (C_{10}-symmetric). Due to the low signal-to-noise ratio of the data set, the detectable separation between neighboring EQCs is weak, thus contributing to the strong two-fold signal at 180° and, similarly, to the weaker autocorrelations that suggest a 10-fold rotational symmetry. Scale bar = 30 nm for (A) and 8 nm for (B,C).

previously reported through the mixing of purified wild-type (WT) gp10 and pRNA.[24]

Here, we study an N-terminal Strep-II/His_6 gp10 extension (N-Strep/His) with the sequence: MWSHPQFEKGGGGGGGGGGAM-HHHHHH-DYDIPTTENLYFQG, which includes a Strep-II tag, a glycine linker followed by a His_6 tag, and a terminal TEV protease site. We determined the stoichiometry and topology of the nanoparticles assembled from recombinant N-Strep/His gp10 *via* transmission electron microscopy (TEM). Through two-dimensional (2D) image analysis and classification, three-dimensional (3D) tomographic and volume reconstructions, and atomic fitting of the reconstructed volumes, we show that purified gp10 N-Strep/His can consistently form self-assembled nanoparticles composed of seven individual recombinant connectors. By orienting their peptide-tagged N-termini into the nanoparticle core, five equatorial connectors and two juxtaposed polar connectors can associate into a metastable heptameric arrangement. Further analysis reveals that each connector is capable of individual degrees of rotational and translational movement while associated with the nanoparticle, likely due to the flexible nature of the Strep/His extensions. Finally, the formation of heptameric nanoparticles with five equatorial connectors appears favored over that of hexameric or octameric nanoparticles (with four or six equatorial connectors, respectively), a stoichiometry likely required for optimal tag-mediated connector aggregation and stabilization.

RESULTS

Nanoparticle Stoichiometry and Topology Determined *via* TEM Image Analysis. To initially characterize the structure of the N-Strep/His nanoparticles, TEM projections were collected and 2D image analysis was performed. As was seen previously with N-terminal Strep-II (N-Strep) or His_6 (N-His) gp10 constructs, stain-embedded N-Strep/His gp10 TEM projections with similar morphology and symmetry were identified (Figure 1A). Projection orientations exhibiting cyclic five-fold-symmetric (C_5) top views and elliptical two-fold-symmetric side views were easily recognized. The elliptical side view projections reveal the presence two orthogonal mirror axes, where two juxtaposed conical densities can be seen at the top and bottom of the projection, as well as another flanking pair on the left and right (Figure 1B). These side views, which measure ~24 nm × 29 nm, share a major axis length that is equal to the ~29 nm diameter of the circular top view projections. The top view projections consist of five equally spaced conical densities arranged around a common rotation axis, with each conical density flanked by regions devoid of density (Figure 1C). The majority of top view projections also contain a ring-like density which coincides with the apparent C_5 axis. Our previous report found that imposition of C_5 symmetry to top view projections of N-Strep gp10 strongly strengthened the signal of the conical densities. From that analysis, it was predicted that the radial densities were contributed by five "equatorial" connectors (EQCs) arranged on their sides, with their narrow N-termini facing into the nanoparticle core. The centralized, circular density was hypothesized to be two opposing "polar" connectors (POCs) arranged in a top view orientation (narrow N-termini inward), with the local POC C_{12} axes coincident with the global nanoparticle C_5 axis. With this prediction, the C_5 symmetry axis degenerates into a pseudo-C_5 axis, as it is coincident with the local POC C_{12} axes. To confirm the pseudo-C_5 top view symmetry with the current N-Strep/His construct, a polar transform (PT) and its autocorrelation were generated from the single, well-resolved top view in Figure 1C. The PT reveals 10 density extensions connected every 72° at lower radii, corresponding to the EQC edges (extensions) and N-terminal neck (connections) (Figure 1D). Additionally, between each connected density extension pair is a region devoid of density, corre-

sponding to the gap between adjacent EQCs. The autocorrelation of the PT reveals peaks every 36°, with more intense peaks occurring every 72° (Figure 1E). These signals also suggest the presence of a pseudo-C_5 symmetry axis and correlate with the predicted configuration of five side-oriented EQCs. Lastly, the generation of 2D class averages from top-view-only projections generated *via* supervised or unsupervised classification resulted only in five-fold-symmetric classes (Figure S1, Supporting Information). Together, these 2D analyses support the notion of a pseudo-C_5 symmetry axis inherent to the nanoparticle structure.

Tomographic and Volume Reconstruction of the Nanoparticle. To confirm the nanoparticle dimensions and heptameric connector stoichiometry determined from the 2D projection images, single-molecule stain-embedded tomograms were generated from single-axis tilt data sets. Despite the appreciable amount of noise present, an oblate spheroid with 10 radial density spokes could be identified, along with concentrated conical densities at each pole. Imposition of C_5 symmetry revealed EQC density profiles that strongly correlated with the conical shape and dimensions of a side-view-oriented connector but washed out the densities of the two POCs; conversely, imposition of C_{12} symmetry strongly strengthened the POC densities, while washing out those for the five EQCs. As expected, the variable effects of symmetry imposition between the EQCs and POCs highlight the symmetry mismatch between the two topologically distinct connector positionings. The C_5-imposed tomogram in Figure 2A reveals the overall dimensions of the nanoparticle, measuring 25.0 nm in height and 30.5 nm in diameter. The height-to-diameter ratio of 0.82 determined here is roughly equivalent to the value of 0.80 previously determined from 2D images of N-His nanoparticles. Fitting of the tomogram with atomic phi29 connector coordinates (PDB 1H5W) reveals that seven connectors can fit precisely into the nanoparticle volume, with five positioned as EQCs and two as POCs (Figure 2B,D), with no remaining contoured volume for additional connectors. The conical nature of the EQCs and the lack of appreciable density within the ~14.0 nm diameter nanoparticle core are highlighted in Figure 2C,D. The EQC height × diameter dimensions of 9.0 nm × 13.5 nm and the POC dimensions of 8.5 nm × 12.5 nm measured within C_5- or C_{12}-symmetrized tomograms, respectively, are in close agreement to the actual connector dimensions of 8.0 nm × 13.5 nm, suggesting that the structures of both the EQCs and POCs are well-preserved upon association into the nanoparticle.

A final confirmation of the recombinant N-Strep/His connector arrangement within the nanoparticle involved the generation of a 3D model constructed *via* multi-image reconstruction from the 2D projection data set. The top view of the reconstruction reveals five well-resolved conical density profiles, corresponding to the

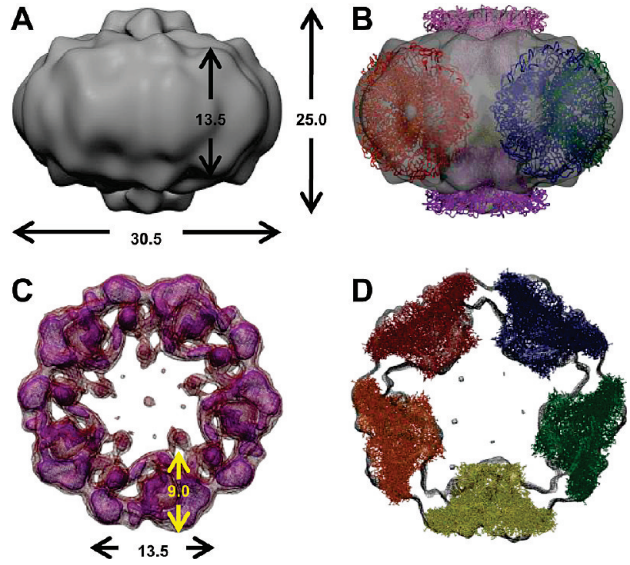

Figure 2. Single-molecule tomographic reconstruction and molecular docking of an isolated nanoparticle. (A) Side view tomogram isosurface rendered at 1.3σ above mean density. The ellipsoidal nanoparticle measures 25.0 nm in height and 30.5 nm in diameter. Two protrusions are present, one at each of the poles, corresponding to the juxtaposed POCs. The height of the central ellipsoidal belt is 13.5 nm, which matches well with the diameter of a single connector. (B) Transparent isosurface rendering of (A), with seven WT gp10 connector coordinates (PDB 1H5W) fit into the reconstruction. A nanoparticle stoichiometry consisting of five EQCs and two POCs is evident. (C) Top view of the tomogram sectioned to reveal only the EQCs, displayed in mesh at three different volume contours. Color scheme from warm to cool reflects high to low contours, respectively. The conical shape profile of the five EQCs is clear, measuring 9.0 nm in height and 13.5 nm in overall diameter. (D) Central section of the top view in (C) with five connectors fit into the reconstruction, revealing the goodness-of-fit of the connector coordinates into their corresponding EQC densities (measurement values in nanometers).

five EQCs, arranged with their narrow ends inward and wider ends outward (Figure 3A). Additionally, a ring-like density corresponding to the POCs is present at the center of this orientation, positioned above the N-terminal regions of the EQCs. Tilting of the volume generates the oblique view in Figure 3B, which allows for better visualization of the oblate nature of the nanoparticle, as well as the two POC densities. Additionally, the central pores of the two front-most EQCs can be seen, along with a distinct separation between them. As with the tomographic reconstruction, interpretation of the nanoparticle as a heptameric connector assembly was further confirmed by the fitting of five EQCs and two POCs into the reconstruction (Figure 3C). The docked connectors occupy the majority of their assigned densities, supporting the fact that each volume segment corresponds to a single dodecameric connector building block. The height × diameter dimensions of the multi-image reconstruction of 24.0 nm × 29.0 nm are in excellent agreement with those from the single-particle tomogram. Within the nanoparticle core, the conical nature of both the EQCs and POCs is easily seen (Figure 4). Interestingly, no appreciable density is found within the core region, even when rendered at low den-

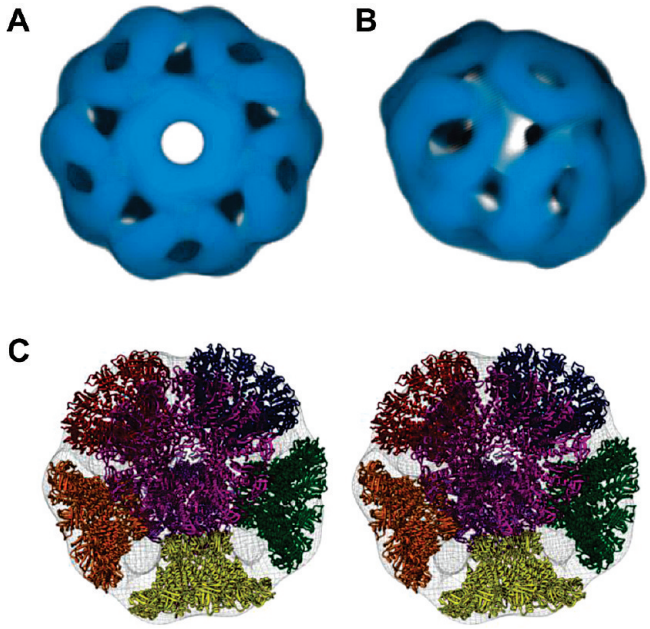

Figure 3. Nanoparticle volume rendering generated from multi-image refinement. (A) Top and (B) oblique views rendered at 1.0σ above mean density. Five EQCs and a centralized POC density can be distinguished in the top view, while two POCs and two full (front-most) and three occluded (rear-most) EQCs can be seen in the oblique view. The nanoparticle dimensions from this single-particle reconstruction measure 24.0 nm in height and 29.0 nm in diameter. (C) Cross-eyed stereomesh rendering of the nanoparticle with molecular docking of seven connector coordinates. Goodness-of-fit of the molecular docking is made evident by the full accommodation of all seven dodecamers into the global density profile. It is assumed that the N-Strep/His connectors have nearly the same atomic structure for docking as the WT gp10 connector.

sity contours. If the N-terminal peptide extensions are located within this region, the lack of a coherent signal strongly suggests their structure to be either random or disordered. Taking the measured edge-to-edge distance between two POCs of 8.0 nm and the distance between opposite EQCs of ~14.0 nm, we calculate a pentagonal void volume of 8.8×10^2 nm^3. Determination of the volume occupied by the 84 Strep/His tags per nanoparticle resulted in a value of 4.5×10^2 nm^3, which is roughly one-half the calculated void volume (Table S1, Supporting Information). Likely, the 84 Strep/His tags have adequate space to interact within the entirety of the nanoparticle core.

Connector Mobility and Packing within the Nanoparticle Assembly. To analyze the structural stability of the nanoparticle, we sought to determine the identity and degree of conformational heterogeneity of the connector substituents. Correspondence analysis applied to all discernible top-view-only projections, which intentionally included particles removed during quality screening, revealed the presence of considerable structural variation.[25,26] The resultant eigenimages suggested that significant amounts of radial translation of the EQCs was possible, along with "top" views that were elliptical in nature. These unique, elliptical projections contained POCs in dead-on top views surrounded by 10 radial density spokes, suggesting additional degrees of EQC rotational freedom into or out of the equatorial plane. These top view projections deviate from the "average" nanoparticle structure reported here, however, as they do not follow the pseudo-C_5 symmetry of untilted, equiradially positioned EQCs used in our model. Further evidence of connector mobility is provided in Figure 5. Individual projections were selected from each of three different top-view-only size classes which were found to exhibit equiradially positioned EQCs (Figure 5A−C). The medium-sized population has dimensions that match those of the volume reconstructions, which we interpret as the average nanoparticle structure. The majority of top-only views contained nanoparticle dimensions consistent with the medium size class, further emphasizing this particular size class as the population average. The small- and large-sized populations can be generated if topological flexibility of the EQCs is allowed (Figure S2, Supporting Information). By translating the EQCs of the medium-size class radially inward, the small-sized population can be generated. In con-

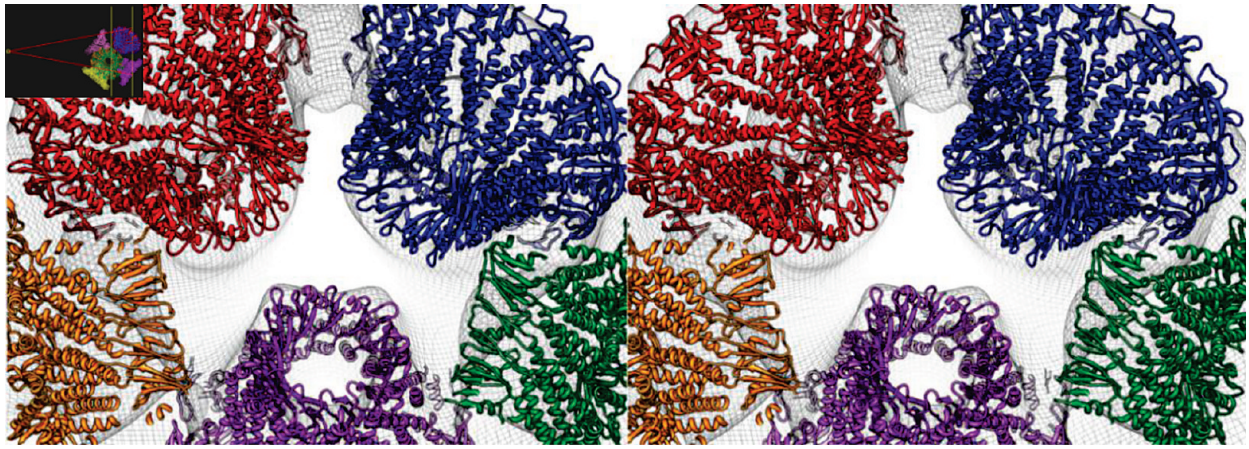

Figure 4. Cross-eyed stereomesh rendering of the nanoparticle interior docked with WT gp10 connector coordinates. The field of view is as depicted in the boxed cross section within the top-left inset. Four EQCs are shown and are colored orange, red, blue, or green, while the bottom POC is colored purple. This interior view within the nanoparticle void volume reveals the likely location of the interacting N-terminal peptide extensions.

trast, the large-size class can be generated by maintaining the radial positioning of the EQCs from the medium-size class, with a concomitant tilting of each EQC into or out of the equatorial plane. The tilting results in an apparent increase in height of the individual EQC projections as they progress toward a more oblique orientation. Illustrative mock-ups for these size class volumes are shown in Figure 5E−G. To confirm these interpretations, pseudoatomic models which mimic the EQC rearrangements for the three size classes were generated (Figure 5I−K). The close agreement between the modeled 2D reprojections and the size-classified data projections support the hypothesis of EQC translational and rotational mobility. The probability of the formation of the small- and large-size classes shown here is extremely small, however. To form the small size class from the population average, all five EQCs must pull inward simultaneously and in equal magnitude, while formation of the large-size class would require all five EQCs to simultaneously tilt into or out of the equatorial plane with similar magnitude. In fact, fewer than 10% of the selected top view projections were found with either the small or large topological arrangements. An example of the individual degrees of freedom experienced by the constituent connectors within a nanoparticle is shown in Figure 5D. This particular nanoparticle exhibits two EQCs (left-most and top-left) that are tilted into/out of the equatorial plane. Additionally, the left-most EQC has translated away from the nanoparticle core to a significant degree, while the top-left EQC has translated away slightly and exhibits a moderate in-equator plane rotation, orienting its N-terminus away from the center of the nanoparticle core. Clearly, the N-terminally extended connectors have numerous, independent degrees of rotational and translational mobility within the nanoparticle assembly.

It is interesting to note that nanoparticles with either four or six EQCs were not readily detected. It follows that the optimal packaging arrangement involves the tight association of five connector constituents capped by two polar connectors. Modeling of four or six EQC nanoparticles reveals that EQC−POC N-terminal tag interactions are likely necessary for stable heptameric nanoparticle formation (Figure 6A and Figure S3 and Table S1 in the Supporting Information). Simultaneous, stabilizing interactions between either POC and all of the EQCs within the 6-EQC model are less probable due to the increased diameter of the EQC belt. Within the 4-EQC model, although both EQC−EQC and EQC−POC interactions appear maintained, it is possible that volume constraints imposed by the tighter EQC belt prevents the efficient accommodation of all 72 tags within the nanoparticle core. Additionally, stability of the 4-EQC structure may be decreased relative to the 5-EQC structure due to having EQCs with looser packing and, therefore, higher mobility. Together, these models suggest that the 5-EQC arrangement determined here displays optimal stabilizing EQC−EQC and EQC−POC interactions, a large enough void volume to cleanly accommodate the N-terminal tags, and close subunit packing that limits destabilizing connector displacements, thus making it the predominately observed nanoparticle species.

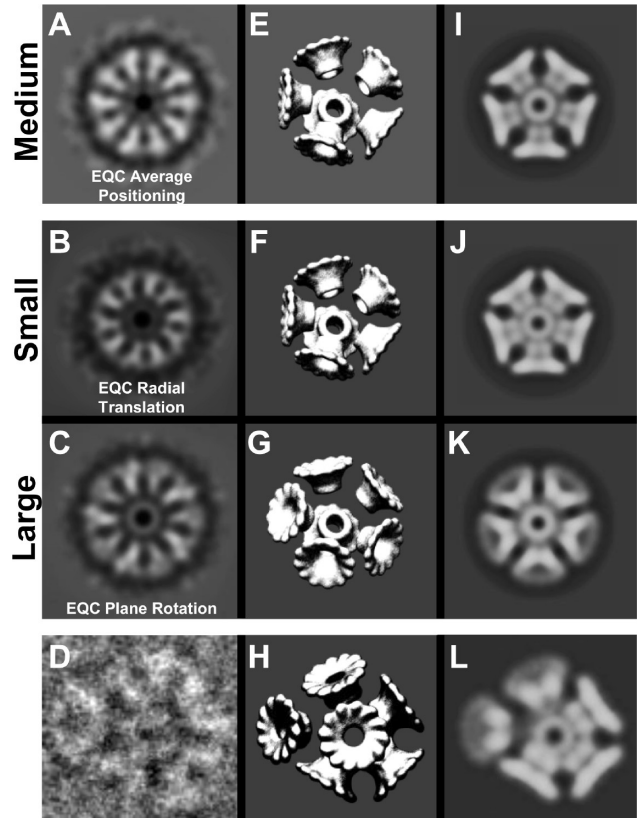

Figure 5. Comparison of nanoparticle top view projections from different size classes. Examples of individual (A) medium, (B) small, and (C) large nanoparticle projections with applied five-fold rotational symmetry. Differences in overall nanoparticle and void diameters are evident, as well as apparent EQC height. Rounding of the connector edges in these projections is likely due to differences in connector in-plane rotation, which inherently blurs the sharp C-terminal boundaries when averaged and symmetrized. Sketch interpretation of the nanoparticle size classes reveals either an inward radial translation or an into/out-of-plane rotation of the EQCs from the medium nanoparticle (E) to generate small (F) or large (G) nanoparticles, respectively. Reprojection of modeled density mock-ups from (E−G) with imposed contrast transfer modulation function reveals the similarity between the actual data projections (A−C) and the modeled interpretations (I−K). A unique nanoparticle projection is shown in (D), revealing the independence of the rotational and translational degrees of freedom exhibited by the left-most and top-left EQCs, in addition to their freedom of mobility independent of the other EQCs. A mock-up of (D) is shown in (H), with reprojection shown in (L). Note: N-terminal residues 1−16 and C-terminal residues 285−309 were not solved within the PDB crystal structure due to their inherent flexibility, which may lead to slight differences during comparison to the data.

DISCUSSION

N-Terminal Extensions Are Responsible for Nanoparticle Formation. In our attempts to create individual gp10 connectors with functionalized N- and C-terminal peptide extensions, we have come across the induced aggrega-

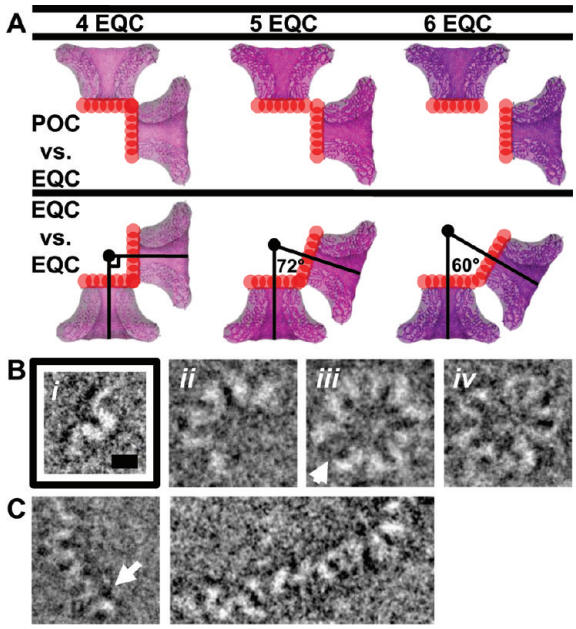

Figure 6. EQC/POC stabilization and nanoparticle intermediates. (A) Comparison of the potential peptide-mediated interactions between the POCs−EQCs and EQCs−EQCs of modeled 4-, 5-, and 6-EQC nanoparticles. The radii of the red spheres correspond to the ~0.9 nm radius of gyration of the 41 amino acid N-Strep/His tags. Stabilizing interactions can be formed between the tags of the POCs and EQCs of the 4- and 5-EQC nanoparticles but are too physically separated in the 6-EQC case. Overlap between neighboring EQCs is present among each of the modeled nanoparticles, despite the differences in angles between neighboring EQCs; however, formation of 4-EQC nanoparticles may be disfavored due to volume packing constraints within the nanoparticle core (Table S1). (B) Nanoparticle intermediates revealing (i) two connectors, (ii) three connectors, (iii) five connectors—open EQC belt, and (iv) five connectors—closed EQC belt. All connectors are oriented with their narrow N-termini facing inward. The intermediate in (iii) reveals a singular, open interface (white arrow), while (iv) exhibits a fully closed EQC belt. Addition of two POCs to (iv) will generate a complete heptameric nanoparticle. (C, left) Three connectors with the bottom-most connector orientation inverted (white arrow). This off-pathway intermediate cannot form a canonical nanoparticle because the curvature required for formation of the EQC belt is negated by the orientation of the bottom-most connector. If this alternating addition of connectors continues (C, right), such a 1D tessellation likely leads to the formation of a 2D connector array. Scale bar = 8 nm.

tion of a heptameric connector complex. This nanoparticle is not formed by WT gp10, as no previous reports have detected its assembly, but is a direct consequence of the N-terminal Strep-II/His extension. We previously showed that removal of the N-terminal peptide through TEV protease cleavage resulted in the spontaneous disassembly of the nanoparticles. Our previous report also established that N-terminal Strep *or* His tags alone are sufficient for nanoparticle formation; however, any such addition to the C-termini of gp10 did not lead to nanoparticle formation. These results are consistent with the tomographic and single-particle reconstructions shown here, whose seven connector N-termini were found to orient into the nanoparticle core. By having all of the extensions oriented into a common volume, the likelihood of interpeptide interactions is greatly increased. The nature of the peptide-mediated interactions specifically responsible for the formation of the nanoparticle remains to be determined, as all nanoparticle-forming N-terminal tags (N-His, N-Strep, and N-Strep/His) tested thus far contain a variety of charged, polar, and hydrophobic residues. Introduction of a variety of chemically streamlined N-terminal extensions onto gp10 will help to further characterize the interactions responsible for induced aggregation. Additionally, the use of length-variant peptide extensions can be generated to test the importance of tag length on nanoparticle stability and connector stoichiometry. Also, generation of sequence-randomized tags can be used to check for the possibility of nonspecific interactions in nanoparticle formation. Finally, a stability-enhanced nanoparticle assemblage can be anticipated through the introduction of cross-links between chemically modified residues, allowing for the formation of covalent intertag linkages. By testing these possibilities, an optimized set of interactions can be tailored toward specific induced assembly or tethering applications. It is worthwhile to mention here the similarity of nanoparticles formed from the mixing of purified WT gp10 connectors and phi29 pRNA. The pRNA has been shown to bind to the N-terminal region of WT connectors, and it is possible that stabilizing inter-pRNA base pairing and/or stacking occurs between neighboring EQCs and POCs, similar to the mechanism proposed here. By taking advantage of the information contained within the base pairs of DNA or RNA, recognition between the complementary bases of protein-associated nucleotides may also be useful in self-assembly applications.

Relationship between Nanoparticle Intermediates and 2D Array Formation. Close inspection of the projection data set reveals novel assemblies which appear to be nanoparticle intermediates (Figure 6B). These assemblages share the common feature of having their constituent connector building blocks oriented with each N-terminus facing one predefined direction and each C-terminus facing the opposite direction. With regards to assembly, the association of two free connectors in the same orientation generates an initial quantized curvature that is required for the progression of nanoparticle formation. Addition of ancillary connectors maintains this curvature until the fifth and final connector is added, forming a transient pentameric EQC belt. The association of two final POCs on the top and bottom of the EQC belt can then complete the formation of a full, heptameric nanoparticle. Failure to follow the initial quantized curvature, *via* connector addition in a head-to-tail fashion, abrogates nanoparticle formation (Figure 6C, left), leading instead to 1D tessellations (Figure 6C, right). Within a majority of the data sets, a small proportion of EQC-only nanoparticle belts was found (Figure 6B, iv), indicating that a pentameric nanoparticle

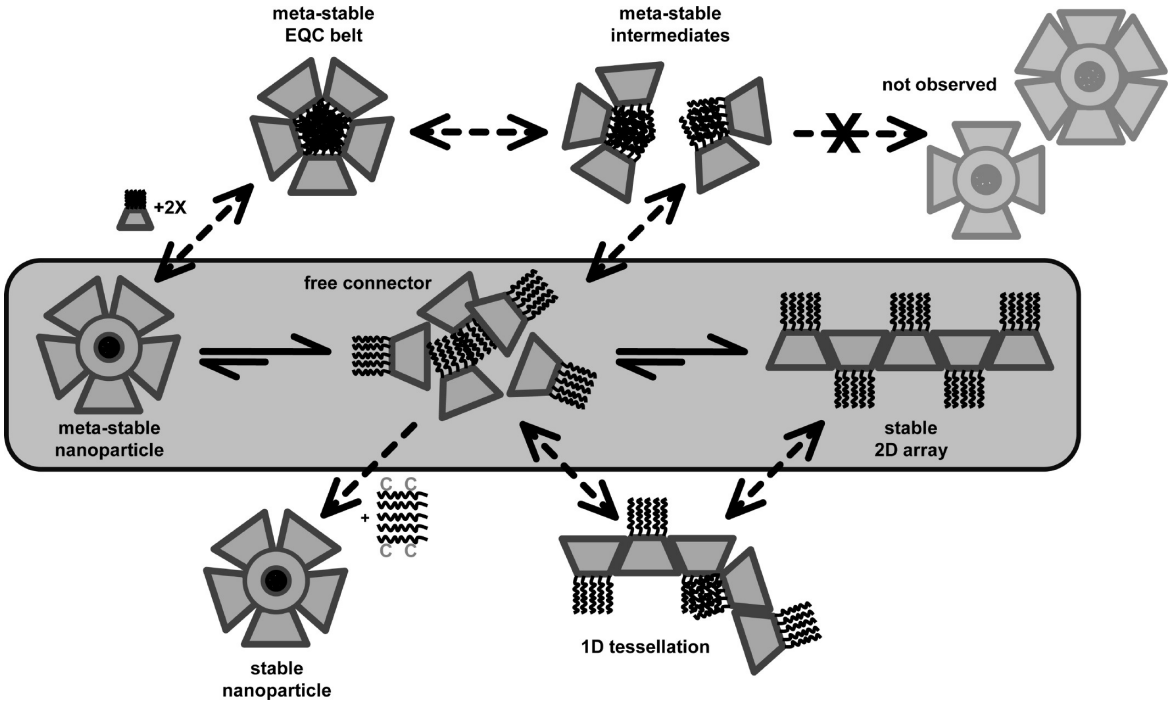

Figure 7. Proposed formation pathway of the heptameric nanoparticles. N-Strep/His connectors in solution are able to form metastable heptameric nanoparticles. Once purified, however, these nanoparticles break down into their constituent connectors and eventually lead to formation of stable 2D connector arrays. This overall pathway is shown within the gray box. From the intermediates shown in Figure 6B, formation of the metastable heptameric nanoparticles likely proceeds through the quantized association of properly oriented N-Strep/His connectors (head-to-head). Eventually, a metastable EQC belt is formed, wherein two polar connectors can associate to form the metastable heptameric end product. From Figure 6A, formation of 4- and 6-EQC nanoparticles is disfavored. Simultaneously, free connectors may begin to associate in an orientation that is not compatible with nanoparticle formation (head-to-tail). These 1D tessellations titrate out free connector, leading to the more thermodynamically stable 2D array end product. The addition of chemical cross-linkers (CC-tags) to the N-terminal tags is envisioned to prevent the formation of the 2D array, leading to stable nanoparticle formation through covalent tag interactions.

state devoid of POCs is a viable, yet weakly stable intermediate. Correspondence analysis of the top-view-only nanoparticles supports the presence of the pentameric connector belt within the heptameric nanoparticle population. The resulting eigenimage reveals a circular area of variation within the center of the top view projections, implicating the variable presence of POCs among the assemblies.[27] In terms of stability, the heptameric structure reported here appears to be a metastable arrangement, as prolonged incubation (weeks to months) of purified samples resulted in the breakdown of the nanoparticles into free connectors and 2D arrays. The arrays that formed were highly resistant to agitation and changes in temperature and, thus, appear to be a thermodynamic end point for both purified WT and N-terminus-tagged connectors.[28] Previous efforts geared toward solving the structure of WT connectors relied on the formation of such 2D arrays. These connector sheets would form from purified connectors quite readily, further suggesting a higher level of stability over free connector in solution. Significantly, purified WT connectors were never found to assemble into the nanoparticles reported here, suggesting an inability to form from WT protein. Through the addition of the N-terminal peptides in this experiment, we have been able to generate nanoparticles that are assembled in a pathway direction which opposes 2D array formation (Figure 7).

CONCLUSION

The requirement of the N-terminal peptide tags in nanoparticle formation discussed here is clear, as their self-assembly from both WT and C-terminal-modified connectors has not been observed. Accordingly, nanoparticle formation is likely the result of a peptide-mediated tethering and stabilization effect. We surmise that the initial action of the N-terminal extensions is to tether connectors within close proximity of one another in an orientation-dependent manner. Upon successful tethering, the shape complementarity of the connector profiles allows for the precise fitting of five EQCs and two POCs into an arrangement suitable for transient, yet stabilizing interconnector interpeptide associations. Flexibility of the peptide tags allows for translational and rotational mobility of the individual connectors; however, the overall heptameric identity of the nanoparticles remains preserved. By applying tailored peptide extensions to other macromolecular systems, the induced formation of similar supramolecular self-assemblies is envisioned.

In addition to using the nanoparticle and its N-terminal tags as a test-bed for peptide-based molecular tethering, subsequent modification of a covalently stabilized nanoparticle with its 84 solvent-accessible C-terminal tags will allow for a number of therapeutic and diagnostic applications.[29−31] Cell-specific targeting can be achieved through C-terminal tag functionalization with various ligands, small molecules, or antibodies designed against membrane-associated receptors or signaling proteins. Additionally, the conjoining of compounds such as enzymatic inhibitors or radiopharmaceuticals can be employed for therapeutic treatments, while the attachment of environment-specific molecular beacons can function as reporters useful for *in vivo* diagnostics and imaging. Finally, simultaneous surface PEGylation can modify the overall hydrophobicity of the nanoparticle, as well as help in immune system evasion and tolerance.[32] By attaching various combinations of surface-exposed moieties, the nanoparticle discussed here with its built-in stoichiometric specificity and combinatorial ligand flexibility can serve as an extensible platform for use in nanotheranostics and nanomedical applications.

METHODS

Construction of gp10 N-Strep/His. Plasmid construction of phi29 gp10 connector with subsequent N- or C-terminal modifications has been described.[22,23,28] For the N-Strep/His connector, the modified gp10 gene was inserted into the *Nde*I-*Xho*I sites of the plasmid vector pET-21a(+) (EMB Biosciences, Madison, WI). PCR was used to amplify the gp10 gene from the phi29 genomic DNA-gp3. Plasmid pGp10-N-Strep/His was constructed from the plasmid pGp10-N-His by ligating a sequence encoding the Strep-II tag to the 5′ of the plasmid (Supporting Information Table 2). The resulting plasmid was confirmed with restriction mapping and sequencing.

Expression and Purification of gp10 N-Strep/His. Plasmid pGp10-N-Strep/His was transformed into *Escherichia coli* strain HMS179 (DE3). Luria−Bertani (LB) medium containing 100 μg/mL ampicillin and induction with 0.5 mM IPTG was employed for cell growth and protein expression. Cells were harvested by centrifugation and frozen at −70 °C until use. Purification of gp10-N-Strep/His was conducted with one-step affinity chromatography by Strep-Tactin (IBA, St. Louis, MO). Cells were resuspended with buffer W (15% glycerol, 500 mM NaCl, 1 mM EDTA, 100 mM Tris-HCl, pH 8.0) and 10−20 column volume of the clarified lysate was loaded to Strep-Tactin Sepharose resin. After washing the column with buffer W, buffer E (15% glycerol, 500 mM NaCl, 1 mM EDTA, 2.5 mM desthiobiotin, 100 mM Tris-HCl, pH 8.0) was used to elute.

TEM Imaging and Tomographic and Single-Particle Reconstructions. The nanoparticles were embedded within a 16% solution of ammonium molybdate in order to generate high-contrast projections while simultaneously avoiding drying-distortion artifacts of traditional negative staining.[33] The use of cryo imaging conditions was precluded by the high salt present within the nanoparticle buffer solution. Single-molecule tomograms were generated from a single-axis tilt data set collected on a 200 kV JEOL-2100 TEM in two-degree increments between −60 and +60° at 24 000× magnification (CCD sampling of 4.12 Å/pixel).[34] Alignment was performed locally to individual nanoparticles with eTomo from IMOD using a cross-correlation metric.[35] The output volume was Gaussian-filtered with a filter width of 10.0 standard deviations, followed by mirroring across its long axis, and C_5-symmetrized using *proc3d* from EMAN.[36] Volume display, coloring, molecular docking, and distance measurements were performed using UCSF Chimera.[37]

To perform the single-particle volume reconstruction, images of stain-embedded nanoparticles were collected at 200 kV on the same TEM at 40 000× magnification (CCD sampling of 2.5 Å/pixel) with a defocus range of ~0.8 to 2.5 μm. Projections were selected from drift- and astigmatism-free micrographs. To limit the effects of conformational heterogeneity on the reconstruction process, only projections which shared a consistent maximum diameter were selected. The images were then low-pass filtered to 20 $Å^{-1}$ to accentuate the individual connector profiles within the nanoparticle. Two different initial models were used to carry out refinement: a common-lines model generated with *startcsym* from the best identified side and top view shown in Figure 1B,C, or the tomographic volume shown in Figure 2. After five to eight rounds of model-based refinement using the *refine* command within EMAN with imposed C_5 symmetry, both of the refinements converged to a similar structure, exhibiting features and dimensions similar to that of the tomographic reconstruction. Next, a 40 $Å^{-1}$ low-pass filtered volume generated from the pseudoatomic tomogram fitting shown in Figure 2B was used as a starting model for model-based refinement without symmetry imposition. Despite the five-fold reduction in symmetry averaging power, 10 rounds of iterative refinement generated a volume with the expected dimensions, along with the presence of 10 radial density spokes. A final reconstruction was starting using the same low-pass filtered pseudoatomic volume as a starting model, along with five-fold symmetry imposition. The final reconstruction was generated after the fifth round from 3720 of 4111 starting particles. Forty classes were generated by using an angular spacing of 10°. To ensure decent class homogeneity, particles outside of $\pm 1.2\sigma$ from the mean cross-correlation value within a class average were discarded. Additionally, class averages whose phase residuals in relation to their corresponding model reprojection greater than 15° were discarded. The resolution is estimated to be 40 $Å^{-1}$ using a Fourier shell correlation cutoff of 0.5 or 32 $Å^{-1}$ using a cutoff of 0.143, similarly done with previously established procedures and with the final reconstruction low-pass filtered to 35 $Å^{-1}$ for visualization purposes.[38,39] Contrast transfer function correction was not performed due to the resolution being limited to well within the first zero of the micrographs with the largest defocus. Resolution was likely limited in the reconstruction due to additional conformational heterogeneity (changes in EQC radial translation or rotation) that was not readily perceptible during manual particle screening or in the later stages of class refinement.

Acknowledgment. We thank R. Díaz-Avalos, E. Baldwin, and L. Domínguez-Ramírez for their helpful suggestions, as well as H. Furukawa and M. Kawasaki for their input of initial data processing. This study was sponsored by NIH (T32-GM08799), Cancer pilot grant and Discovery Fund, as well as fellowships provided by Lawrence Livermore National Laboratory (D.J.G., DE-AC52-07NA27344) and by National Science Council (J.C.W.).

Supporting Information Available: Supplemental Figures S1−S3 and Supplemental Tables 1 and 2. This material is available free of charge *via* the Internet at http://pubs.acs.org.

REFERENCES AND NOTES

1. Branco, M. C.; Schneider, J. P. Self-Assembling Materials for Therapeutic Delivery. *Acta Biomater.* **2009**, *5*, 817–831.
2. Kentsis, A.; Borden, K. L. Physical Mechanisms and Biological Significance of Supramolecular Protein Self-Assembly. *Curr. Protein Pept. Sci.* **2004**, *5*, 125–134.
3. Steinmetz, N. F.; Lin, T.; Lomonossoff, G. P.; Johnson, J. E. Structure-Based Engineering of an Icosahedral Virus for Nanomedicine and Nanotechnology. *Curr. Top. Microbiol. Immunol.* **2009**, *327*, 23–58.
4. Worrall, J. A.; Gorna, M.; Pei, X. Y.; Spring, D. R.; Nicholson, R. L.; Luisi, B. F. Design and Chance in the Self-Assembly of Macromolecules. *Biochem. Soc. Trans.* **2007**, *35*, 502–507.

5. Zhang, S. Fabrication of Novel Biomaterials through Molecular Self-Assembly. *Nat. Biotechnol.* **2003**, *21*, 1171–1178.
6. Clark, J.; Singer, E. M.; Korns, D. R.; Smith, S. S. Design and Analysis of Nanoscale Bioassemblies. *Biotechniques* **2004**, *36*, 992−996; 998−1001.
7. Palmer, L. C.; Velichko, Y. S.; de la Cruz, M. O.; Stupp, S. I. Supramolecular Self-Assembly Codes for Functional Structures. *Philos. Trans. A* **2007**, *365*, 1417–1433.
8. Guo, P.; Grimes, S.; Anderson, D. A Defined System for *In Vitro* Packaging of DNA-gp3 of the *Bacillus subtilis* Bacteriophage Phi29. *Proc. Natl. Acad. Sci. U.S.A.* **1986**, *83*, 3505–3509.
9. Colombo, G.; Soto, P.; Gazit, E. Peptide Self-Assembly at the Nanoscale: A Challenging Target for Computational and Experimental Biotechnology. *Trends Biotechnol.* **2007**, *25*, 211–218.
10. Namba, K. Roles of Partly Unfolded Conformations in Macromolecular Self-Assembly. *Genes Cells* **2001**, *6*, 1–12.
11. Ulijn, R. V.; Smith, A. M. Designing Peptide Based Nanomaterials. *Chem. Soc. Rev.* **2008**, *37*, 664–675.
12. Reilly, B. E.; Spizizen, J. Bacteriophage Deoxyribonucleate Infection of Competent *Bacillus subtilis*. *J. Bacteriol.* **1965**, *89*, 782–790.
13. Ramirez, G.; Mendez, E.; Salas, M.; Vinuela, E. Head-Neck Connecting Protein in Phage Phi29. *Virology* **1972**, *48*, 263–265.
14. Carrascosa, J.; Carazo, J.; Garcia, N. Structural Localization of the Proteins of the Head to Tail Connecting Region of Bacteriophage Phi29. *Virology* **1983**, *124*, 133–143.
15. Guasch, A.; Pous, J.; Ibarra, B.; Gomis-Ruth, F. X.; Valpuesta, J. M.; Sousa, N.; Carrascosa, J. L.; Coll, M. Detailed Architecture of a DNA Translocating Machine: The High-Resolution Structure of the Bacteriophage Phi29 Connector Particle. *J. Mol. Biol.* **2002**, *315*, 663–676.
16. Valpuesta, J. M.; Fernandez, J. J.; Carazo, J. M.; Carrascosa, J. L. The Three-Dimensional Structure of a DNA Translocating Machine at 10Å Resolution. *Structure* **1999**, *7*, 289–296.
17. Guo, P. X.; Erickson, S.; Anderson, D. A Small Viral RNA Is Required for *In Vitro* Packaging of Bacteriophage Phi29 DNA. *Science* **1987**, *236*, 690–694.
18. Shu, D.; Guo, P. Only One pRNA Hexamer but Multiple Copies of the DNA-Packaging Protein gp16 Are Needed for the Motor To Package Bacterial Virus Phi29 Genomic DNA. *Virology* **2003**, *309*, 108–113.
19. Lee, T. J.; Schwartz, C.; Guo, P. Construction of Bacteriophage Phi29 DNA Packaging Motor and Its Applications in Nanotechnology and Therapy. *Ann. Biomed. Eng.* **2009**, *37*, 2064–2081.
20. Wendell, D.; Jing, P.; Geng, J.; Subramaniam, V.; Lee, T. J.; Montemagno, C.; Guo, P. Translocation of Double-Stranded DNA through Membrane-Adapted Phi29 Motor Protein Nanopores. *Nat. Nanotechnol.* **2009**, *4*, 765–772.
21. Moll, D.; Huber, C.; Schlegel, B.; Pum, D.; Sleytr, U. B.; Sara, M. S-Layer-Streptavidin Fusion Proteins as Template for Nanopatterned Molecular Arrays. *Proc. Natl. Acad. Sci. U.S.A.* **2002**, *99*, 14646–14651.
22. Cai, Y.; Xiao, F.; Guo, P. The Effect of N- or C-Terminal Alterations of the Connector of Bacteriophage Phi29 DNA Packaging Motor on Procapsid Assembly, pRNA Binding, and DNA Packaging. *Nanomedicine* **2008**, *4*, 8–18.
23. Xiao, F.; Cai, Y.; Wang, J. C.; Green, D.; Cheng, R. H.; Demeler, B.; Guo, P. Adjustable Ellipsoid Nanoparticles Assembled from Re-engineered Connectors of the Bacteriophage Phi29 DNA Packaging Motor. *ACS Nano* **2009**, *3*, 2163–2170.
24. Tsuprun, V.; Anderson, D.; Egelman, E. H. The Bacteriophage Phi29 Head−Tail Connector Shows 13-Fold Symmetry in Both Hexagonally Packed Arrays and as Single Particles. *Biophys. J.* **1994**, *66*, 2139–2150.
25. Frank, J.; van Heel, M. Correspondence Analysis of Aligned Images of Biological Particles. *J. Mol. Biol.* **1982**, *161*, 134–137.
26. van Heel, M.; Frank, J. Use of Multivariate Statistics in Analysing the Images of Biological Macromolecules. *Ultramicroscopy* **1981**, *6*, 187–194.
27. White, H. E.; Saibil, H. R.; Ignatiou, A.; Orlova, E. V. Recognition and Separation of Single Particles with Size Variation by Statistical Analysis of Their Images. *J. Mol. Biol.* **2004**, *336*, 453–460.
28. Xiao, F.; Sun, J.; Coban, O.; Schoen, P.; Wang, J. C.; Cheng, R. H.; Guo, P. Fabrication of Massive Sheets of Single Layer Patterned Arrays Using Lipid Directed Reengineered Phi29 Motor Dodecamer. *ACS Nano* **2009**, *3*, 100–107.
29. Nanda, P. K.; Lane, S. R.; Retzloff, L. B.; Pandey, U. S.; Smith, C. J. Radiolabeled Regulatory Peptides for Imaging and Therapy. *Curr. Opin. Endocrinol. Diabetes Obes.* **2010**, *17*, 69–76.
30. Surendiran, A.; Sandhiya, S.; Pradhan, S. C.; Adithan, C. Novel Applications of Nanotechnology in Medicine. *Indian J. Med. Res.* **2009**, *130*, 689–701.
31. Lee, S.; Xie, J.; Chen, X. Peptide-Based Probes for Targeted Molecular Imaging. *Biochemistry* **2010**, *49*, 1364–1376.
32. Abuchowski, A.; McCoy, J. R.; Palczuk, N. C.; van Es, T.; Davis, F. F. Effect of Covalent Attachment of Polyethylene Glycol on Immunogenicity and Circulating Life of Bovine Liver Catalase. *J. Biol. Chem.* **1977**, *252*, 3582–3586.
33. Harris, J. R.; Scheffler, D. Routine Preparation of Air-Dried Negatively Stained and Unstained Specimens on Holey Carbon Support Films: A Review of Applications. *Micron* **2002**, *33*, 461–480.
34. Soonsawad, P.; Xing, L.; Milla, E.; Espinoza, J. M.; Kawano, M.; Marko, M.; Hsieh, C.; Furukawa, H.; Kawasaki, M.; Weerachatyanukul, W.; *et al.* Structural Evidence of Glycoprotein Assembly in Cellular Membrane Compartments Prior to Alphavirus Budding. *J. Virol.* **2010**, *84*, 11145–11151.
35. Kremer, J. R.; Mastronarde, D. N.; McIntosh, J. R. Computer Visualization of Three-Dimensional Image Data Using IMOD. *J. Struct. Biol.* **1996**, *116*, 71–76.
36. Ludtke, S. J.; Baldwin, P. R.; Chiu, W. EMAN: Semiautomated Software for High-Resolution Single-Particle Reconstructions. *J. Struct. Biol.* **1999**, *128*, 82–97.
37. Pettersen, E. F.; Goddard, T. D.; Huang, C. C.; Couch, G. S.; Greenblatt, D. M.; Meng, E. C.; Ferrin, T. E. UCSF Chimera—A Visualization System for Exploratory Research and Analysis. *J. Comput. Chem.* **2004**, *25*, 1605–1612.
38. Xing, L.; Li, T; Miyazaki, N.; Simon, M. N.; Wall, J. S.; Moore, M; Wang, C; Takeda, N; Wakita, T; Miyamura, T; *et al.* Structure of Hepatitis E Virion-Sized Particle Reveals an RNA-Dependent Viral Assembly Pathway. *J. Biol. Chem.* **2010**, *285*, 33175–33183.
39. Kawano, M.; Xing, L.; Tsukamoto, H.; Inoue, T.; Handa, H.; Cheng, R. H. Calcium-Bridge Is Required To Trigger Capsid Disassembly over Cell Entry Process of Simian Virus 40. *J. Biol. Chem.* **2009**, *284*, 34703–34712.